Materials Views

www.MaterialsViews.com

ADVANCED
ENERGY
MATERIALS

www.advenergymat.de

COMMUNICATION

Enhancing the Kinetics of Li-Rich Cathode Materials through the Pinning Effects of Gradient Surface Na+ Doping

Ren-Peng Qing, Ji-Lei Shi, Dong-Dong Xiao, Xu-Dong Zhang, Ya-Xia Yin, Yun-Bo Zhai,* Lin Gu,* and Yu-Guo Guo*

Lithium-ion batteries have been widely applied in electric vehicles (EVs) and hybrid electric vehicles (HEVs) owing to their high power density and high energy density.[1–3] Among the cathode materials for lithium-ion batteries, lithium-rich layered materials of $Li_2MnO_3 \cdot LiMO_2$ (M = Mn, Ni, Co, Fe, Cr, etc.) have attracted wide attention because of their high specific capacity (up to 250 mA h g^{-1}), low cost, and high safety.[4–8] However, they suffered from the poor electrode kinetics and underwent large voltage decays during repeated cycles, thus leading to the inferior rate capacity and poor cycling stability.[6] The kinetics could become even worse for lithium-rich materials with large dense particles. In recent years, much effort has been paid to surface stabilization, such as doping,[9–12] heterostructuring,[13–15] and coating,[16–19] to overcome these issues that plague their practical implementation. The challenge faced with Li-rich layered materials in volumetric energy density requires the usage of large dense particles with high discharge capacity.[20,21] However, due to the poor kinetics of the large particles, partial activation of Li_2MnO_3 phase usually exists with cycling, and needs several cycles to realize the full-activation. This electrochemical activation process could deteriorate their reversible capacity and hinder their further application.[20,22]

Numerous investigations have revealed that the electrochemical activity of Li_2MnO_3 is relevant to the degree of its structure defects, and higher degree of structure defects could facilitate the electrochemical activity of Li_2MnO_3.[22–24] Conventional approaches in activating Li_2MnO_3 component in Li-rich layered materials are mainly through chemical etching of Li_2O in Li_2MnO_3 phases to generate structural defects, such as nitric acid or hydrazine hydrate modification.[6,20,25] Although Li_2MnO_3 could be activated, which improved the initial Coulombic efficiency, the original surface morphology is prone to being destroyed during the etching process (Figure S1a, Supporting Information), hence leading to the poor cycling stability (Figure S1b, Supporting Information) and rate performance during subsequent cycles. Li-rich layered materials modified by hydrazine hydrate was reported to have long-term energy retention.[20] However, the unfavorable platform below 3.0 V appears in the discharge process, which compromises the energy density, especially for the Mn-rich based Li-rich cathode materials (Figure S2, Supporting Information).

Xia and co-workers reported to improve their electrochemical performances through controlled structure defects in Li_2MnO_3 phase of Li-rich materials.[26] However, a high degree of structure defects, accompanied with highly disordering of Li$^+$ in the transition metal layer, would deteriorate the structural stability, leading to the poor cycling stability and the rate capacity. Na$^+$ doping has been reported to be an effective avenue to facilitate the Li$^+$ diffusion of Li-rich layered materials and thus to improve their rate capacity.[27–30] Note that it is vital to control the doping amount of Na$^+$. Li-rich layered materials doped with a low amount of Na$^+$ would exhibit the poor cycling stability whereas the material doped with a high amount of Na$^+$ shows decreased specific capacity and deteriorates the energy density.[28] Therefore, it is still challenging to develop one simple and effective approach to synthesize Li-rich layered material with much improved kinetics.

Herein, we propose a novel method to enhance the kinetics of large particle Li-rich layered materials by gradient surface Na$^+$ doping. Driven by Na$^+$ concentration diffusion thermodynamically, gradient surface Na$^+$ doping are realized through the calcination process of Li-rich materials in molten NaCl state. Powder X-ray diffraction (XRD) shows that high degree of structure defects are formed in Li_2MnO_3 phase of Li-rich material in molten NaCl flux.[26] Gradient Na$^+$ doping on the surface of large particle Li-rich layered material could not only realize the pinning effect in stabilizing the Li-rich layered structure with large amount of structural defects but also facilitate the diffusion of Li$^+$ in the layered structure. Accordingly, the resultant large particle Li-rich layered material represents superior electrochemical performances, particularly high specific capacity, excellent Coulombic efficiency, and impressive cycling stability. The schematic illustration of the structural design is shown in **Figure 1**.

R.-P. Qing, J.-L. Shi, X.-D. Zhang,
Dr. Y.-X. Yin, Prof. Y.-G. Guo
Key Laboratory of Molecular Nanostructure
and Nanotechnology
Beijing National Laboratory for Molecular Science
Institute of Chemistry
Chinese Academy of Sciences (CAS)
Beijing 100190, P. R. China
E-mail: ygguo@iccas.ac.cn

R.-P. Qing, Prof. Y.-B. Zhai
College of Environmental Science and Engineering
Hunan University
Changsha 410082, P. R. China
E-mail: ybzhai@hnu.edu.cn

D.-D. Xiao, Prof. L. Gu
Beijing National Laboratory for Condensed Matter Physics
Institute of Physics
Chinese Academy of Sciences (CAS)
Beijing 100190, P. R. China
E-mail: l.gu@iphy.ac.cn

Prof. Y.-G. Guo
Shandong Wina Green Power Co. Ltd.
Shouguang 262705, P. R. China

**ADVANCED
ENERGY
MATERIALS**

www.advenergymat.de

*Materials
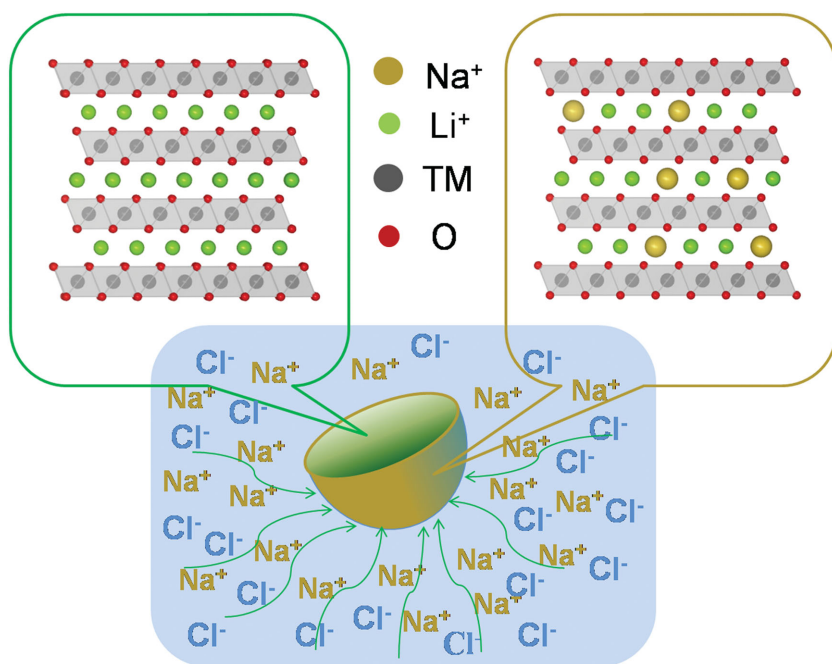Views*

www.MaterialsViews.com

COMMUNICATION

Figure 1. Schematic illustration of the structure design of gradient surface Na+ doping Li-rich material.

Figure 2 shows scanning electron microscopy (SEM) images and XRD patterns of the pristine Li-rich material (PLR) and gradient surface Na+ doped Li-rich material (SLR). The SEM images of the materials indicate the spherical morphology of the precursor and lithium-rich cathode materials (Figure 2a–c). Both the PLR and SLR materials are dense microsized particles. The size distribution of the carbonate precursor examined by laser particle analyzer is D10 = 11.5 μm, D50 = 18.6 μm, and D90 = 29.2 μm (Figure S3, Supporting Information). The XRD patterns of the PLR and SLR material could be indexed to the R-3m space group of the layered α-NaFeO$_2$ structure and

C-2m space group of Li$_2$MnO$_3$ (Figure 2d).[15] After doping, the (003) and (104) peaks of SLR, shown in Figure 2e,f, are shifted to lower angle, which means enlargement in Li+ slab.[10,29] To gain the quantitative data of the lattice parameter, Rietveld refinement of the XRD data was conducted and shown in Figure S4 (Supporting Information). The calculated lattice parameters are listed in **Table 1**. Both crystal parameters a and c of SLR are larger than that of PLR, which means the lattice expansion in both a and c directions after Na+ doping. As shown in Figure 2g, 2-theta range from 20° to 25°, relating to the superlattice of Li$_2$MnO$_3$ phase, of SLR differed from that of PLR apparently. The SLR material exhibits only one single broad peak, while the PLR material exhibits two sharp peaks. The broadening of the superlattice peaks in the 2-theta range of 20°–25° was reported to correspond to the increased degree of stacking faults of Li$_2$MnO$_3$.[22,24,26] The local changes in the occupation of O atoms would change stacking sequence of LiMn$_2$ planes, thereby creating stacking faults.[31] Molten salt flux calcination method could control the stacking faults of Li-rich materials as reported by Xia and co-workers.[26] Moreover, metal oxygen layers were pushed apart at the occupation sites of Na atoms, which would also change the local environment of O atoms.[30] These might suggest that the occupation sites of O atoms in Li$_2$MnO$_3$ phase would be slightly different after calcinations in the molten NaCl flux, and thereby induces stacking faults.

To analyze the surface component of the material, X-ray photoelectron spectroscopy (XPS) of PLR and SLR materials were performed and shown in **Figure 3**. The XPS spectra of manganese 2p$_{1/2}$ at 654 eV and 2p$_{3/2}$ at 642 eV correspond to the
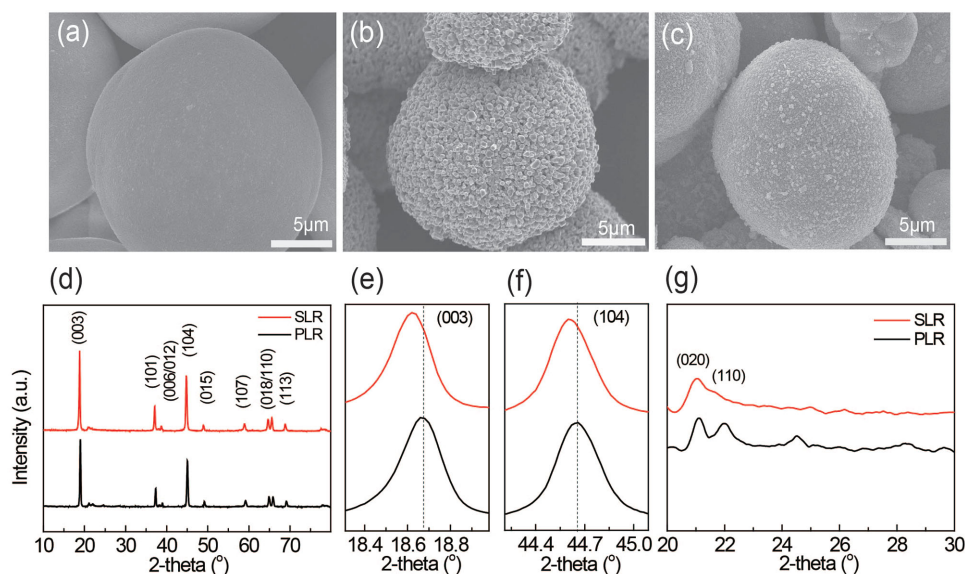

Figure 2. SEM images of a) carbonate precursor, b) PLR, and c) SLR. d–g) XRD patterns of PLR and SLR.

www.MaterialsViews.com

ADVANCED
ENERGY
MATERIALS
www.advenergymat.de

COMMUNICATION

Table 1. Refined crystal parameters of PLR and SLR. Targeted space group was selected as R-3m.

Materials	a [Å]	c [Å]	c/a ratio	Refinement parameters
PLR	2.84501	14.2069	4.9936	Rwp: 5.66; Rp: 4.01
SLR	2.84865	14.2268	4.9942	Rwp: 5.26; Rp: 3.64

MnO_2 and they are identical for both PLR and SLR, suggesting the same oxidation state of Mn, in these two materials.[14,26] However, compared to that of PLR, the binding energy of Ni 2p and Co 2p of SLR are slightly shifted to the high level, suggesting that the oxidation state of Ni and Co are slightly higher on the surface of SLR. The slightly increased oxidation state of Ni and Co might be relevant to the calcination process. For SLR, XPS spectrum of Na 1s is detected on the material surface, while no Cl is observed (Figure S5, Supporting Information). This indicates that Na^+ is doped into the surface of the material, rather than the physical adsorption of the residual NaCl without washing completely. To confirm the gradient Na^+ doping in the material surface, XPS spectra in depth were performed (Figure 3d). As the increase of detection depth, the intensity of Na 1s spectra decreases, corresponding to the gradient Na^+ distribution from the material surface to the inside. The atomic percent of Na^+ was 0.4025% at the surface, equivalent to the Li-rich formula $Li_{1.2-x}Na_xM_{0.8}O_2$ (x represents the mole ratio of Na, M represents the transition metals) with $x = 0.1101$. The detected atomic percent of Na decreased to 0.2703% at 3.5 nm and finally reduced to 0.1340% at 31.2 nm, which correspond to $x = 0.0584$ and $x = 0.0279$ in the formula, respectively. The detailed atomic percent of Na^+ detected by XPS spectra in various depths was summarized in Table S1 (Supporting Information). To better understand the structural evolution of SLR, in situ XRD patterns were collected at different temperature during the calcination process (Figure S6, Supporting Information). Detailed discussions concerning the evolution of the material are provided in the Supporting Information.
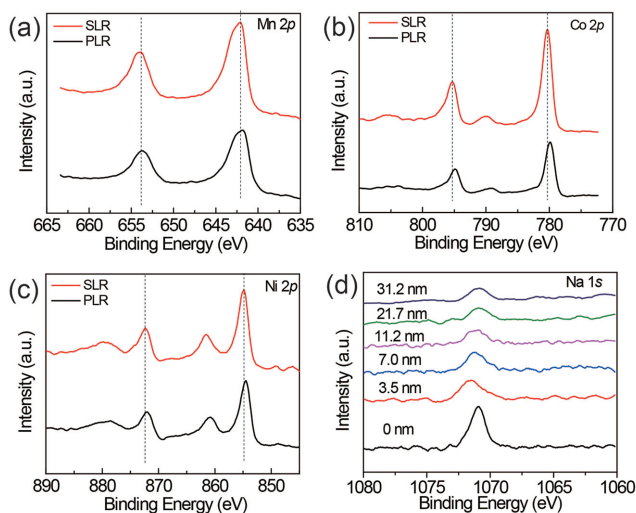
Moreover, aberration-corrected scanning transmission electron microscopy (STEM) of SLR was conducted, shown in **Figure 4**, to gain an insight into its structure at the atomic scale. One could clearly see the layered structure with high degree of crystallization from the high-angle annular-dark-field (HAADF) and corresponding annular-bright-field (ABF) images along the [010] orientation of SLR (Figure 4a,b).[31,32] Since HAADF-STEM imaging is sensitive to heavy elements, Figure 4a shows no observable contrast in Li slab, suggesting that no cation mixing between Li^+ and TM ions exists in SLR. Thereby, we can preclude the influence of TM ions on the contrast of Li slab. It is well-established that ABF-STEM imaging is sensitive to light elements and the intensity of atom columns in ABF images is proportional to the averaged atom number of element.[32,33] Therefore, compared to the pure Li column without Na occupation, when Na^+ occupies the Li sites and the averaged atom number increases, the higher atomic number of Na compared to Li would exhibit the higher intensity in Na-doped lithium atom columns. From this perspective, the higher peaks in the intensity profile along the Li slab imply the Na occupation in this column clearly (Figure 4c). STEM images of SLR with different areas were also conducted which show well consistency (Figure S7, Supporting Information). And they were further compared with the STEM images of PLR to confirm doping sites of Na^+ in SLR. Based on the analysis of STEM results and previous literature,[30] we suggest the Na^+ occupation in the Li^+ slab, as marked by arrow in Figure 4c and Figure S7 (Supporting Information).

The electrochemical performances of PLR and SLR are shown in **Figure 5**. When cycled at the current density at 0.1 C (1 C = 250 mA g^{-1}) from 2.0 to 4.7 V at room temperature, the discharge capacity of PLR is 187 mA h g^{-1} at first cycle and progressively increases to 206 mA h g^{-1} in the second cycle and then to 228 mA h g^{-1} in the fifth, which is typically an electrochemical activation process. Due to the activation process during cycling, the initial Coulombic efficiency of the pristine Li-rich cathode material is only 63%. However, the SLR shows discharge capacity of 286 mA h g^{-1} and Coulombic efficiency of 87% at first cycle, both much higher than that of PLR. After five cycles, discharge capacity of SLR still maintains 286 mA h g^{-1} and no obvious electrochemical activation process is observed during subsequent cycling (Figure 5b). Figure 5c compares the initial charge–discharge curves of PLR and SLR at 0.1 C. The charge capacity of SLR below 4.4 V is 114 mA h g^{-1}, higher than that of PLR (104 mA h g^{-1}). The delithiation potential of SLR is 3.68 V, lower than that of PLR (3.80 V) from their CV curves (Figure S8, Supporting Information). All these indicate the easier diffusion of Li^+ in the layered structure of SLR. Furthermore, the rate performance of SLR is significantly enhanced in contrast with PLR (Figure 5d). SLR material shows much high rate performance with 286 mA h g^{-1} at 0.1 C, 265 mA h g^{-1} at 0.2 C, 236 mA h g^{-1} at 0.5 C, 215 mA h g^{-1} at 1 C, and 185 mA h g^{-1} at 2 C, whereas PLR delivers the discharge capacity of 228 mA h g^{-1} at 0.1 C (after fully electrochemical activation), 204 mA h g^{-1} at 0.2 C, 177 mA h g^{-1} at 0.5 C, 154 mA h g^{-1} at 1 C, and 128 mA h g^{-1} at 2 C (Figure S9, Supporting Information). To better understand the dynamic characters of two materials, the electrochemical impedance spectra (EIS) of PLR and SLR were conducted and shown in Figure S10 (Supporting Information). Compared with PLR electrode, SLR electrode
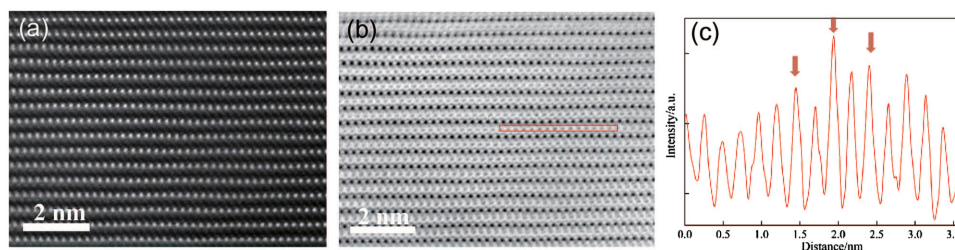

Figure 3. a–c) XPS results of Mn 2p, Co 2p, and Ni 2p of PLR and SLR. d) XPS results of Na 1s in various depths of SLR.

ADVANCED
ENERGY
MATERIALS
www.advenergymat.de

Materials
Views
www.MaterialsViews.com

Figure 4. STEM of SLR surface along [010] zone axis: a) HAADF image, b) ABF image, and c) ABF line profile.

shows lower charge transfer and diffusion (Warburg impedance) resistance which might be beneficial to its rate performance. Figure 5e shows the cycling stability of PLR and SLR materials at 0.2 C. The PLR exhibits a long electrochemical activation process for about 12 cycles, while the SLR delivers high

capacity at 0.2 C without activation process. After 100 cycles at 0.2 C, the SLR exhibits a capacity of 233 mA h g^{-1} much higher than that of PLR (195 mA h g^{-1} after 100 cycles at 0.2 C). To confirm the pinning of Na$^+$ in the Li layer, STEM experiments with ABF line profile for the fully charged SLR sample were
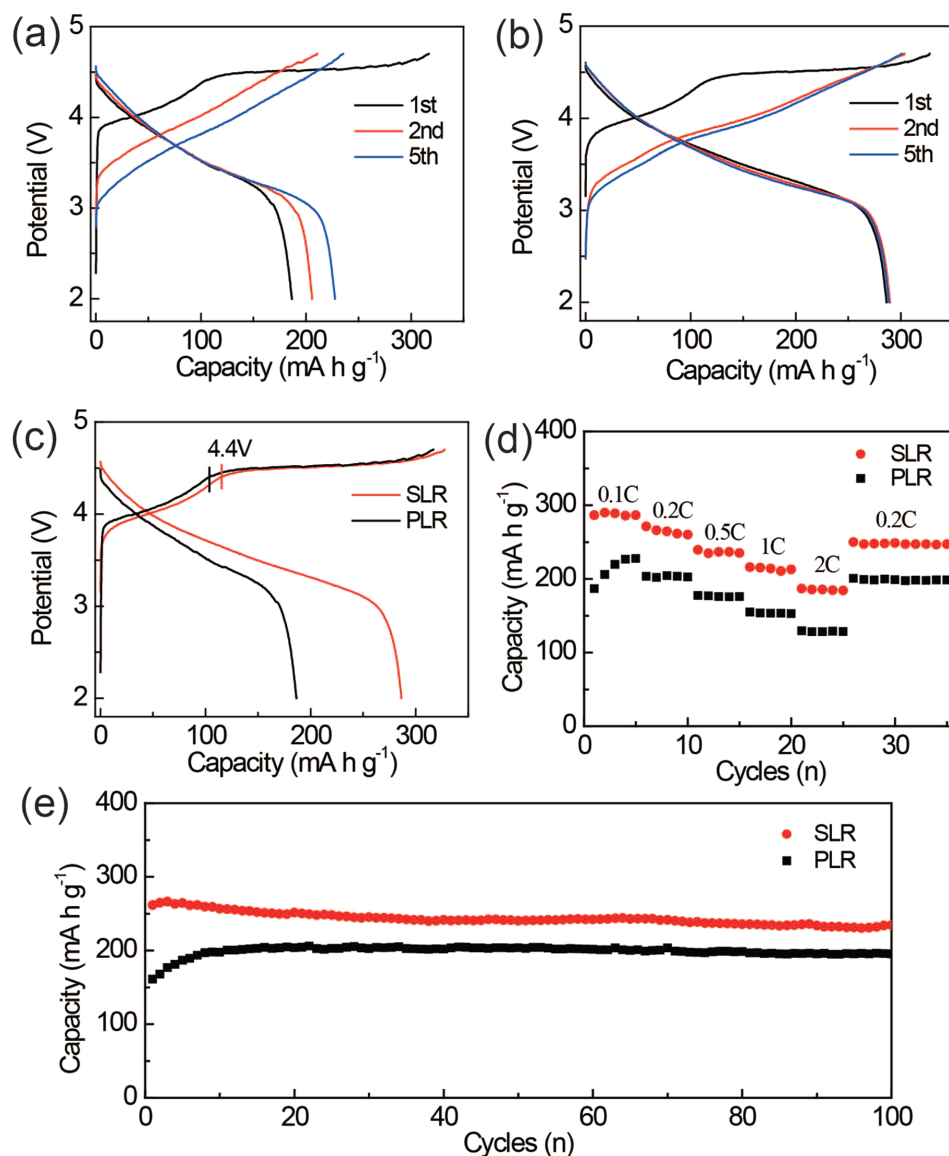

Figure 5. a,b) The charge–discharge curves of the PLR and SLR at 0.1 C, respectively. c) The rate performance and d) cycling stability tested at 0.2 C of PLR and SLR; all of them were tested at 25 °C with voltage ranging from 2 to 4.7 V versus Li$^+$/Li.

www.MaterialsViews.com

ADVANCED
ENERGY
MATERIALS
www.advenergymat.de

COMMUNICATION

conducted and shown in Figure S11 (Supporting Information). From the ABF line profile, we can infer that Na ions still exist in the Li layer after fully charged.

In summary, we have developed a novel gradient doping method in enhancing the kinetics of Li-rich cathode material with high specific capacity (286 mA h g^{-1} at current density of 25 mA g^{-1} coupled with high initial Coulombic efficiency of 87% at room temperature), good cycling stability, and superior rate capability. Confirmed from the results of XRD, XPS, and STEM, we propose that gradient Na$^+$ doping in the surface of the material could realize the pinning effect in stabilizing the structure, and facilitates the diffusion of Li$^+$ in the layered structure, as well as increases the electronic and ionic conductivity of Li-rich materials. The novel method and remarkable electrochemical performances of resultant Li-rich cathode material would promote our understanding in designing high-capacity cathode material for lithium-ion batteries.

Experimental Section

Synthesis of Carbonate Precursor: The carbonate precursor was prepared via a coprecipitation method. 2 M aqueous solution of MnSO$_4$.2H$_2$O, NiSO$_4$.6H$_2$O, CoSO$_4$.7H$_2$O (Mn:Ni:Co molar ratio of 0.54:0.13:0.13) and 2 M Na$_2$CO$_3$ solution containing 0.2 M NH$_3$.H$_2$O were pumped into a 5 L continuous stirred tank reactor simultaneously with the pH kept at 8.1 and the temperature kept at 60 °C. The coprecipitated particles were filtered, washed, and dried at 120 °C for 24 h.

Synthesis of PLR: The pristine cathode material (0.5Li$_2$MnO$_3$.0.5Li Ni$_{1/3}$Co$_{1/3}$Mn$_{1/3}$O$_2$) was prepared by heating stoichiometrically mixed carbonate precursor and Li$_2$CO$_3$ (5% excess of lithium to compensate for lithium loss during the calcination) at 500 °C for 5 h and 850 °C for 12 h at the heating rate of 5 °C min^{-1}. After that the material was cooled to room temperature naturally.

Synthesis of SLR: The activated cathode material was prepared in NaCl flux via molten-salt method. NaCl flux was prepared by mixing a stoichiometric amount of Li$_2$CO$_3$ and Mn—Ni—Co oxide precursor and appropriate amount of NaCl. After homogenously mixing, the mixture was heated to 850 °C in air for 12 h with a heating rate of 5 °C min^{-1}. After that the material was cooled to room temperature naturally and then washed with distilled water for several times and then filtered and dried at 120 °C for 24 h. The Mn—Ni—Co oxide precursor was prepared by calcining carbonate precursor at 500 °C for 5 h with a heating rate of 5 °C min^{-1}.

Structural Characterization: XRD measurements of the powder were performed using a Philips PW3710 with filtered Cu Kα radiation (Rigaku D/max-2500). SEM (JEOL 6701F, operating at 10 kV) was used to investigate the morphology of the obtained material. HAADF and ABF images were obtained with cold field-emission gun and double hexapole Cs correctors (CEOS GmbH, Heidelberg, Germany) STEM (JEOL, Tokyo, Japan) operated at 200 kV and the attainable spatial resolution defined by the probe-forming objective lens was better than 80 pm. XPS was performed on the Thermo Scientific ESCALab 250Xi using 200 W monochromated Al Kα radiation.

Electrochemical Measurements: Electrochemical measurements were performed using coin 2032 cells assembled in an argon-filled glovebox. A mixture of active material, carbon black (CB), and poly(vinyl difluoride) (PVDF) at a weight ratio of 80:10:10 was pasted on an Al foil to prepare the working electrodes. The specific capacity of the hybrid is calculated based on the mass of Li-rich cathode material. The loading mass of the active material on the electrode was 3.0–4.0 mg cm^{-2}. Pure lithium foil was used as a counter electrode. Celgard 2300 film was used as the separator. The electrolyte consisted of a solution of 1 M LiPF$_6$ in ethylenecarbonate (EC)/dimethylcarbonate (DMC)/diethylcarbonate (DEC) (1:1:1 in wt%) obtained from Tianjing Jinniu Power Sources Material Co. Ltd. Galvanostatic cycling of the assembled cells was carried out using an Arbin BT2000 system between the voltage limits of 2.0–4.7 V (vs Li$^+$/Li). Cyclic voltammetry (CV) was performed at 0.05 mV s^{-1} from 2.0 to 4.8 V and EIS was measured in the frequency range from 100 kHz to 10 mHz. Both the CV and EIS were carried out on an Autolab PG302N at room temperature.

Supporting Information

Supporting Information is available from the Wiley Online Library or from the author.

[1] J. M. Tarascon, M. Armand, *Nature* **2001**, *414*, 359.

[2] J. B. Goodenough, K.-S. Park, *J. Am. Chem. Soc.* **2013**, *135*, 1167.

[3] Y.-G. Guo, J.-S. Hu, L.-J. Wan, *Adv. Mater.* **2008**, *20*, 2878.

[4] N. Yabuuchi, K. Yoshii, S.-T. Myung, I. Nakai, S. Komaba, *J. Am. Chem. Soc.* **2011**, *133*, 4404.

[5] H. Yu, H. Zhou, *J. Phys. Chem. Lett.* **2013**, *4*, 1268.

[6] M. M. Thackeray, S.-H. Kang, C. S. Johnson, J. T. Vaughey, R. Benedek, S. A. Hackney, *J. Mater. Chem.* **2007**, *17*, 3112.

[7] M. M. Thackeray, C. Wolverton, E. D. Isaacs, *Energy Environ. Sci.* **2012**, *5*, 7854.

[8] M. S. Whittingham, *Chem. Rev.* **2004**, *104*, 4271.

[9] M. Sathiya, A. M. Abakumov, D. Foix, G. Rousse, K. Ramesha, M. Saubanère, M. L. Doublet, H. Vezin, C. P. Laisa, A. S. Prakash, D. Gonbeau, G. VanTendeloo, J. M. Tarascon, *Nat. Mater.* **2015**, *14*, 230.

[10] Y. Wang, Z. Yang, Y. Qian, L. Gu, H. Zhou, *Adv. Mater.* **2015**, *27*, 3915.

[11] Y. X. Wang, K. H. Shang, W. He, X. P. Ai, Y. L. Cao, H. X. Yang, *ACS Appl. Mater. Interfaces* **2015**, *7*, 13014 .

[12] Q. Li, G. Li, C. Fu, D. Luo, J. Fan, L. Li, *ACS Appl. Mater. Interfaces* **2014**, *6*, 10330.

[13] Y.-K. Sun, Z. Chen, H.-J. Noh, D.-J. Lee, H.-G. Jung, Y. Ren, S. Wang, C. S. Yoon, S.-T. Myung, K. Amine, *Nat. Mater.* **2012**, *11*, 942.

[14] F. Wu, N. Li, Y. Su, H. Shou, L. Bao, W. Yang, L. Zhang, R. An, S. Chen, *Adv. Mater.* **2013**, *25*, 3722.

[15] K.-C. Jiang, X.-L. Wu, Y.-X. Yin, J.-S. Lee, J. Kim, Y.-G. Guo, *ACS Appl. Mater. Interfaces* **2012**, *4*, 4858.

[16] X. Li, J. Liu, M. N. Banis, A. Lushington, R. Li, M. Cai, X. Sun, *Energy Environ. Sci.* **2014**, *7*, 768.

[17] S.-T. Myung, K. Izumi, S. Komaba, Y.-K. Sun, H. Yashiro, N. Kumagai, *Chem. Mater.* **2005**, *17*, 3695.

[18] Y.-K. Sun, M.-J. Lee, C. S. Yoon, J. Hassoun, K. Amine, B. Scrosati, *Adv. Mater.* **2012**, *24*, 1192.

[19] P. Oh, M. Ko, S. Myeong, Y. Kim, J. Cho, *Adv. Energy Mater.* **2014**, *4*, 1400631 .

[20] P. Oh, S. Myeong, W. Cho, M.-J. Lee, M. Ko, H. Y. Jeong, J. Cho, *Nano Lett.* **2014**, *14*, 5965.

ADVANCED
ENERGY
MATERIALS
www.advenergymat.de

www.MaterialsViews.com

COMMUNICATION

[21] X. Yu, Y. Lyu, L. Gu, H. Wu, S.-M. Bak, Y. Zhou, K. Amine, S. N. Ehrlich, H. Li, K.-W. Nam, X.-Q. Yang, *Adv. Energy Mater.* **2014**, *4*, 1300950.

[22] D. Y. W. Yu, K. Yanagida, Y. Kato, H. Nakamura, *J. Electrochem. Soc.* **2009**, *156*, A417.

[23] S.-H. Kang, C. S. Johnson, J. T. Vaughey, K. Amine, M. M. Thackeray, *J. Electrochem. Soc.* **2006**, *153*, A1186.

[24] A. Boulineau, L. Croguennec, C. Delmas, F. Weill, *Solid State Ionics* **2010**, *180*, 1652.

[25] W. C. West, J. Soler, M. C. Smart, B. V. Ratnakumar, S. Firdosy, V. Ravi, M. S. Anderson, J. Hrbacek, E. S. Lee, A. Manthiram, *J. Electrochem. Soc.* **2011**, *158*, A883.

[26] J. Liu, M. Hou, J. Yi, S. Guo, C. Wang, Y. Xia, *Energy Environ. Sci.* **2014**, *7*, 705.

[27] S. H. Park, S. S. Shin, Y. K. Sun, *Mater. Chem. Phys.* **2006**, *95*, 218.

[28] B. Qiu, J. Wang, Y. Xia, Y. Liu, L. Qin, X. Yao, Z. Liu, *J. Power Sources* **2013**, *240*, 530.

[29] S. N. Lim, J. Y. Seo, D. S. Jung, W. Ahn, H. S. Song, S.-H. Yeon, S. B. Park, *J. Alloys Compd.* **2015**, *623*, 55.

[30] M. N. Ates, Q. Jia, A. Shah, A. Busnaina, S. Mukerjee, K. M. Abraham, *J. Electrochem. Soc.* **2014**, *161*, A290.

[31] R. Wang, X. He, L. He, F. Wang, R. Xiao, L. Gu, H. Li, L. Chen, *Adv. Energy Mater.* **2013**, *3*, 1358.

[32] L. Gu, D. Xiao, Y.-S. Hu, H. Li, Y. Ikuhara, *Adv. Mater.* **2015**, *27*, 2134.

[33] Y. Sun, L. Zhao, H. Pan, X. Lu, L. Gu, Y.-S. Hu, H. Li, M. Armand, Y. Ikuhara, L. Chen, X. Huang, *Nat. Commun.* **2013**, *4*, 1870.